DISCLAIMER

LA-UR-25-28805

Approved for public release; distribution is unlimited.

Title: Modeling Volumetric Energy Deposition- driven Rayleigh-Taylor Instability

Author(s): Turner, Benjamin Jack
Zambrano, Noah Claude
Timko, Allyson Brooke
Wilson, Brandon Merrill
Thrussell, Jasper

Intended for: Report

Issued: 2025-08-27

Modeling Volumetric Energy Deposition-driven Rayleigh-Taylor Instability

computational physics summer workshop

Benjamin J. Turner, Noah C. Zambrano

Allyson B. Timko, Brandon M. Wilson, Jasper Thrussell

LA-UR-25-xxxx
August 11, 2025

Los Alamos
NATIONAL LABORATORY

Prepared for: Department
Office
NameTitle
Org

Prepared by: NameTitle
Org

Approvals:

Name	Title	Signature	Date

Contents

Contents

Figures

Tables

1 Introduction

The goal of this work is to simulate a volumetric energy deposition (VED) driven Rayleigh-Taylor instability (RTI). Efforts will focus on simulating effects observed in two-fluid VED-driven RTI experiments [11], [13]. The VED triggers the RTI by changing the density of the fluids through time, hence a variable Atwood number is achieved. While initially stable (heavier fluid on the bottom), the microwave heating creates a density inversion and leads to a RTI. We hope to explore the mechanisms in VED-driven RTI and see how initial perturbations change the dynamics of growth. This work will primarily focus on early-time behavior but will also include steps towards simulating late-time nonlinear behavior.

1.1 Motivation

Buoyancy-driven instabilities, such as the RTI, present significant challenges in engineering applications, including inertial confinement fusion (ICF) and metal casting [12]. In ICF, imperfections in the manufacturing of the capsules can seed RTI growth during compression, potentially limiting or prohibiting ignition due to an uneven implosion. A deeper understanding of the mechanisms driving the RTI is therefore critical for improving target performance and maximizing energy yield of ICF.

Since the conditions present in ICF are very difficult to replicate in a laboratory setting, it has been increasingly important to accurately model the physical behavior, though it is difficult to validate these simulations with experimental references. Simplified experiments of VED RTI have been done using microwaves to trigger the instability [11] [13]. These can help us understand the different dynamics of VED-driven RTI compared to classical RTI and provides a way to verify if the simulations/models are matching reality.

1.2 Dynamics

In VED-driven RTI, the main physical phenomena of interest is variable-Atwood number RTI. However, this brings about various other types of physical processes that impact the flow evolution. Important processes such as heat conduction between different materials bring about potential Rayleigh-Bénard convection (RBC) cells, and multi-modal effects can lead to shearing of different fluids which cause Kelvin-Helmholtz instabilities. Late time behavior becomes nonlinear and eventually transitions to turbulence. These are all problems on their own and require special attention. In this section, we will go over these physical phenomena to guide the modeling efforts and ensure we capture all relevant physics.

The RTI is classically caused by a misalignment of the density gradient and an acceleration field, such as gravity, i.e. $\nabla\rho \times \nabla p \neq 0$. A perturbed interface leads to baroclinic instability and grows over time. The instability is typically parameterized by the Atwood number

$$\mathrm{At}(t) = \frac{\rho_T(t) - \rho_B(t)}{\rho_T(t) + \rho_B(t)}, \tag{1}$$

figure 1-1 shows an unstable fluid configuration (positive Atwood number) and the misalignment of the pressure and density gradients which grow the initial perturbation. In VED-driven RTI, the Atwood number changes with time. This is done by varying one or two fluid densities with time by adding a volumetric heat source. This brings about additional effects which are arguably

Introduction

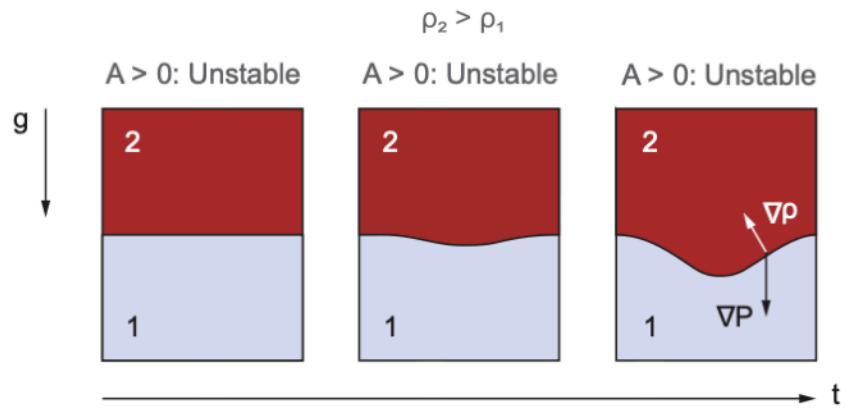

Figure 1-1: Classical Rayleigh-Taylor instability [1]

more important than the RTI itself. The change in temperatures introduce a temperature gradient between the two fluids, which is the key driver for RBC. In RBC, heat flows from the hot fluid to the colder fluid. This forms a local thermal boundary layer in each fluid. For point of reference, suppose the top fluid is denser and colder than the bottom fluid. If the temperature difference becomes large enough in the thermal boundary layer of the colder fluid, the portion of the cold fluid at the bottom becomes less dense due to heating and starts to rise. If this buoyant force overcomes viscous and diffusive resistance, convection sets in. A pattern forms and creates Bénard convection rolls, in which warmer parts of the cold dense fluid rises in the center of a cell, spreads out at the top, cools, and sinks along the edges. This can be important in VED-driven RTI because the

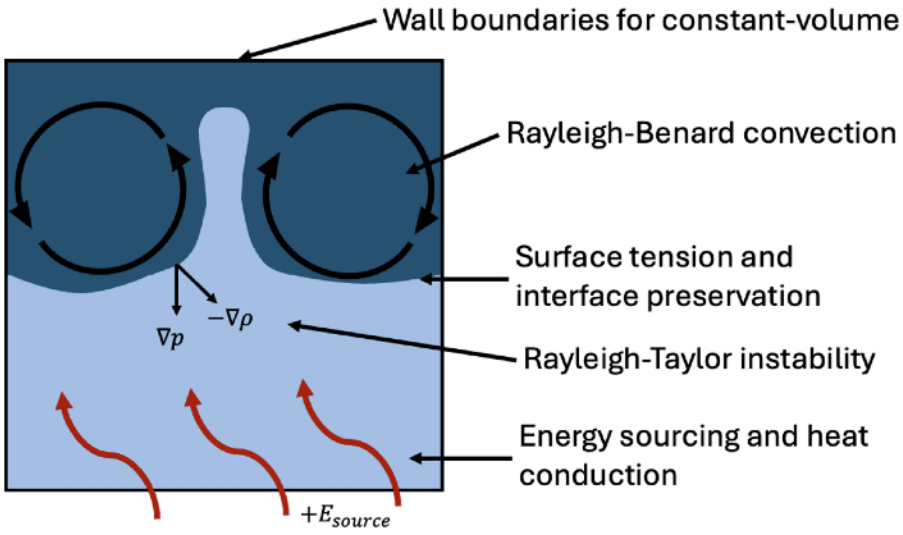

Figure 1-2: Relevant physics for VED-driven RTi.

convection rolls, if formed correctly, can increase the growth rate by “necking" the instability with the motion of the fluid, as shown in figure 1-2. Finally, it is also important to note that at later times, the fluid flow may display a large range of scales, characteristic of turbulent flow, even for

immiscible fluids. Onset of turbulence is quicker in miscible fluids. A turbulent field is shown in figure 1-3, where even at 1 microsecond, the length scales are disparate. In immiscible fluids, the surface tension helps delay turbulence by reducing the growth rate (this is explained in the stability theory section of this report). However, it is not completely avoidable, as it was seen visually in the experiment by Root et al. [11], and even more so in miscible liquids VED-driven RTI experiments such as Wachtor [13].

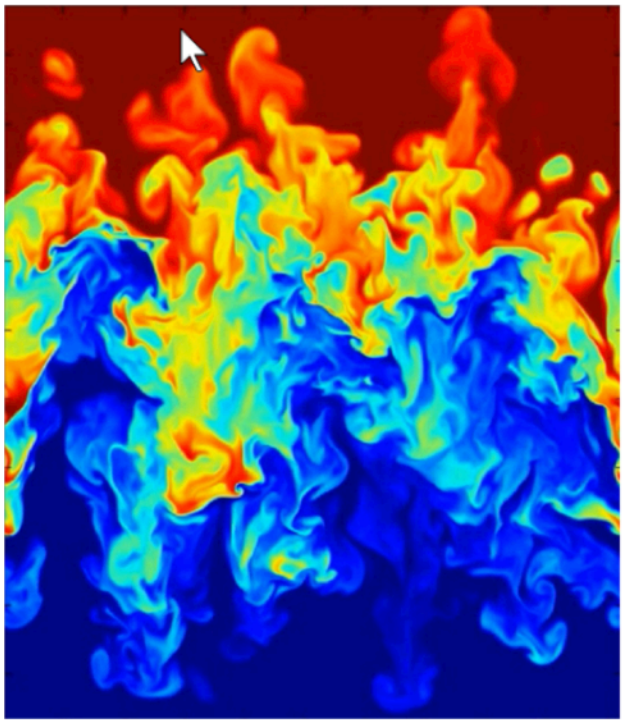

Figure 1-3: RTI with transition to turbulence at large times, from DNS of [9]

1.3 Experiment of interest

The experiment this work aims at replicating is a VED-driven RTI of soybean oil and silicone oil (PDMS), as described in [11]. It is emphasized that exact replication is likely impossible in the internship time frame due to lack of equation of state tables for these two fluids. Regardless, we describe the experiment to guide the initial input creation.

In the experiment, a borosilicate container of volume 7 cm x 7 cm x 12.1 cm was used to reduce dielectric loss with a volume large enough to ignore viscous boundary layer effects on the RTI (boundary layer with the walls). The container was completely filled with the fluid to prevent liquid-air boundary surface waves from interfering with the RTI between the two liquids. The fluids of interest were selected due to their immiscibility and density inversion when subject to microwave heating. For this to happen, the bottom fluid must decrease in density faster than the top fluid. This is characterized by the expandability index which depends on the properties' dielectric loss, density, specific heat, and thermal expansion coefficient. Soybean oil and silicone oil (PDMS) were chosen because both had similar microwave penetration depth (which reduces heating non-uniformity) and different microwave expandability, $2.15 \cdot 10^{-5}$ m^3/kJ and $4.07 \cdot 10^{-5}$ m^3/kJ,

respectively. Interfacial surface tension was also measured in [11]. The interfacial surface tension was experimentally measured using a floating lens approach. It was measured at an average value of 0.45 ± 10.12 mN/m between $20 - 70°$C. Finally, a 1D thermal simulation was used to confirm that the fluid configuration would develop an RTI. The density change was computed for each fluid using

$$\rho(T,z)C_p(T,z)\frac{\partial T}{\partial t} = \kappa(T,z)\frac{\partial^2 T}{\partial z^2} + 2\pi f \epsilon_0 \epsilon''(T,z)E^2. \tag{2}$$

where the T and B subscripts denote top and bottom fluids (as oriented at time=0).

2 Methodology

We now outline the methodology used to simulate the VED-driven RTI. An Eulerian code, xRage [4], is used to simulate the RTI. A brief overview of the governing equations and how the code solves the PDEs is explained, along with case-specific implementation details, such as EOS, energy source, heat conduction, and surface tension.

2.1 Governing equations and solver

The xRage code [4] is a finite-volume code and uses directionally-split hydrodynamics algorithm to solve the compressible Euler equations. It also includes adaptive mesh capabilities to resolve fine, dynamic details. Cell fluxes are computed with a MUSCL-Hancock algorithm and include an acoustic Riemann solver. The states in the Riemann solver are calculated using linear reconstruction to maintain both spatial and temporal second-order accuracy. The two-fluid compressible Euler equations are the set of governing equations that xRage solves. The primitive variables of interest are the micro-densities of each material ρ_1, ρ_2, velocity components u_i in the i^{th} direction, pressure p, and the total energy $E = \frac{1}{2}u_i u_i + e$. The Euler equations consist of the conservation of mass, momentum, and energy.

$$\frac{\partial \alpha_1 \rho_1}{\partial t} + \frac{\partial}{\partial x_i}(\alpha_1 \rho_1 u_i) = 0, \tag{3}$$

$$\frac{\partial \alpha_2 \rho_2}{\partial t} + \frac{\partial}{\partial x_i}(\alpha_2 \rho_2 u_i) = 0, \tag{4}$$

$$\frac{\partial (\rho u_j)}{\partial t} + \frac{\partial}{\partial x_i}(\rho u_i u_j + p\delta_{ij}) = \rho g_i, \tag{5}$$

$$\frac{\partial \rho E}{\partial t} + \frac{\partial}{\partial x_i}\left[u_i(\rho E + p)\right] = \rho u_i g_i \tag{6}$$

where g_i is the gravitational acceleration in the i^{th} direction and α_k is the volume fraction of the k^{th} material. The relationship between the micro-densities, volume fractions, mass fractions μ_k, material specific volume V_k, and specific volume $V = 1/\rho$ is given by

$$\alpha_k = \frac{\mu_k V_k}{V} \tag{7}$$

volume fractions are not advected and instead are used to give the mean density of a cell through

$$\rho = \sum_{k=2}^{2} \alpha_k \rho_k \tag{8}$$

These equations are unclosed by themselves. In order to close them, a relationship between thermodynamic variables must be established. This is done by the equation of state.

2.2 Equation of state

The equation of state provides closure to the compressible Euler equations by relating thermodynamic variables. Since the fluids of interest are liquids, the common EOS of ideal gas is not valid.

However, it can be used to simulate a VED-driven RTI easily, as the density change is always controlled by change in volume and not pressure/temperature. The ideal gas law is

$$p = \rho R T \tag{9}$$

where R is the universal gas constant. If we are trying to replicate the experiment exactly, the correct temperatures/pressures are required and a complete EOS must be provided. A complete equation of state specifies the temperature and the specific entropy as a function of thermodynamic variables, usually given in tabular form for pressure and specific internal energy as functions of specific volume (or density) and temperature $p = p(\nu, T),\ e = e(\nu, T)$. The EOS must provide the material-dependent internal energies e_i and specific volumes such that mean values can be computed through

$$\nu = \sum_{i=1}^{2} \mu_i \nu_i(p, T),\ e = \sum_{i=1}^{2} \mu_i e_i(p, T) \tag{10}$$

xRage solves the system of equations in each mixed cell using an iterative bisection method as described in [4].

2.3 Surface tension and immiscibility

Surface tension and immiscibility are modeled using methodology described in [7]. They are required when the two fluids cannot physically mix together and form an emulsification instead of a mixture. Surface tension is incorporated through source terms in the Euler equations for momentum and energy,

$$\frac{\partial(\rho u_j)}{\partial t} + \frac{\partial}{\partial x_i}(\rho u_i u_j + p\delta_{ij}) = \rho g_i + \sigma\kappa\frac{\partial \alpha_1}{\partial x_i}, \tag{11}$$

$$\frac{\partial \rho E}{\partial t} + \frac{\partial}{\partial x_i}\left[u_i(\rho E + p)\right] = \rho u_u g_i + \sigma\kappa\frac{\partial \alpha_1}{\partial x_i}u_i \tag{12}$$

where σ is a surface tension coefficient and κ is curvature. The interface between fluids is preserved using the volume of fluid (VOF) method, which determines a piecewise-linear interface reconstruction that preserves sharp material interfaces for mass advection calculation [2, 10].

2.4 Internal energy source

VED is implemented by adding a source term to the energy equation. This source term is the time-integrated specific internal energy increase due to microwave heating. All energy is put into the bulk material/electron field and fluid properties are used to compute the microwave power absorption.

$$\frac{de}{dt} = \frac{2\pi f \epsilon_0 \epsilon''(T, z) E^2}{\rho(T, z)} \tag{13}$$

where $\epsilon_0 = 8.854 \times 10^{-12}$(F/m) is the vacuum permittivity, ϵ'' is the dielectric loss coefficient, E is the electric field strength (V/m), f is the microwave frequency (Hz), and ρ is the density of the fluid (g/cm^3).

Choosing an appropriate energy deposition rate for a given set of simulation parameters (e.g., simulation time, initial thermodynamic conditions, etc.) can be nontrivial and often involves trial and error. To mitigate this difficulty, a simplified model describing the evolution of both pressure

and density as a function of the internal energy deposition, assumed to be constant in time and uniform in space for each fluid, can be useful for providing semi-quantitative predictions prior to running a full scale simulation. The following model assumes a single, homogeneous ideal gas, where thermodynamic properties are spatially uniform and the adiabatic index γ is constant. In the case of VED-induced Rayleigh–Taylor instability (RTI), this model must be applied separately to each species in the system. Using the equation of state for an ideal gas, the density of the fluid can be written as a function of its specific internal energy and pressure.

$$\rho = \frac{p}{e\,(\gamma - 1)} \tag{14}$$

Differentiating equation 14 with respect to time results in the relationship between the change in density in terms of changes in pressure and specific internal energy.

$$\frac{d\rho}{dt} = (\gamma - 1)^{-1} \left(\frac{1}{e}\frac{dp}{dt} - \frac{p}{e^2}\frac{de}{dt} \right) \tag{15}$$

From ideal gas, the time derivative of pressure is proportional to the change in internal energy scaled by a factor of $\gamma - 1$.

$$\frac{dp}{dt} = (\gamma - 1)^{-1} \left(\frac{d\,(\rho e)}{dt} \right) = (\gamma - 1)^{-1} \left(e\frac{d\rho}{dt} + \rho\frac{de}{dt} \right) \tag{16}$$

Substituting the relation in equation 16 into equation 15 gives the time derivative of density purely in terms of the change in specific internal energy.

$$\frac{d\rho}{dt} = (\gamma - 1)^{-2} \left(\frac{d\rho}{dt} + \frac{\rho}{e}\frac{de}{dt} \right) - (\gamma - 1)^{-1} \left(\frac{p}{e^2}\frac{de}{dt} \right) \tag{17}$$

Rearranging the implicit form of equation 17 results in an explicit expression for the time rate of change of density, written solely in terms of the change in specific internal energy and the system's current state. Substituting this result back into equation 16 similarly produces an explicit expression for the time evolution of pressure.

$$\frac{d\rho}{dt} = \frac{1}{\gamma\,(\gamma - 2)} \left(\frac{\rho}{e} - \frac{p\,(\gamma - 1)}{e^2} \right) \frac{de}{dt} \tag{18}$$

$$\frac{dp}{dt} = \frac{1}{(\gamma - 1)} \left(\frac{1}{\gamma\,(\gamma - 2)} \left(\rho - \frac{p\,(\gamma - 1)}{e} \right) + \rho \right) \frac{de}{dt} \tag{19}$$

Once an initial state is specified, these two equations 18-19 are numerically solved simultaneously at each time step to update the thermodynamic state of the system in response to energy deposition. This simplified model enables rapid evaluation of how a given initial state evolves over time, which is especially useful for estimating the required internal energy source strength to flip the Atwood number of the system.

2.5 Heat conduction

Heat conduction is the transfer of thermal energy through matter, from a region of higher temperature to a region of lower temperature [6]. It can be described as heat energy transferred from one volume of material to another by direct contact. In VED-driven RTI, the two different fluids at

different temperatures are in contact at the interface and thus have heat transfer. Typically, the Euler-equations are not suitable for this as thermal conductivity is set to zero, but xRage includes options to include heat conduction.

Heat conduction is accomplished through the bulk material/electron, denoted 2T and 3T modes, respectively. For this problem, we only care about the material heat conduction. The PDE that is solved is

$$\rho c_v \frac{\partial T}{\partial t} = \frac{\partial}{\partial x_i}\left[\kappa(\rho, T)\frac{\partial T}{\partial x_i}\right] \tag{20}$$

where c_v is the specific heat at constant volume and $\kappa(\rho, T)$ is the thermal coefficient. The coefficient is found using an analytic power law

$$\kappa_m = \kappa_0 \left(\frac{T_{ion}}{T_{ref}}\right)^{N_{temp}} \rho_m^{N_\rho} \tag{21}$$

where T_{ion} is the ion temperature, κ_0 is the thermal coefficient for conduction, N_{temp} is the exponent for temperature power law, T_{ref} is the reference temperature for temperature power law, and N_ρ exponent for density power law. If only κ_0 is specified, then $\kappa_m = \kappa_0$ for all temperatures and densities. Thermal conductivity was held constant for each material to simplify everything and since density/temperature changes are small. This equation is solved implicitly for stability at large time steps. In mixed (multi-material) cells, κ is calculated by averaging the values of κ_m for all materials using the averaged state values.

2.6 Fluid Selection

Fluid selection plays a pivotal role in determining the dynamics of the RTI, particularly in systems involving time-dependent VED. Unlike classical RTI with a constant Atwood number, where the density gradient is externally fixed, VED creates local temperature changes that dynamically alter the density field with time. Therefore, extra consideration must be given to the relationship between temperature, pressure, and density, since the density gradient must flip from a stable to an unstable configuration to trigger a RTI. The requirement for immiscibility further constrains fluid choices to liquids, as gases are typically miscible. In addition multiphase systems involving phase transitions are often dominated by diffusion and latent heat effects rather than interfacial instability dynamics, so we avoid conditions that introduce multiphase effects.

Most conventional liquids exhibit low compressibility and weak thermal expansion, meaning their density does not change significantly with temperature. This limits their usefulness in simulations and experiments of VED driven RTI, where the changing density gradient is required to drive RT growth. To combat this, choosing two liquids with similar density at the same thermodynamic state, i.e. matching pressure and temperature, minimizes the total energy required to flip the density gradient through heating. Additional consideration must be made to ensure that both fluids remain in liquid phase throughout the total duration of energy deposition, since phase changes will obscure the study of the interface instability. Some oils, liquid hydrocarbons and molten polymers are generally more compressible than water and have comparable densities when in liquid state.

In xRage, the SESAME tables must be used for the equation of state closure of liquids. However, there were no oil tables available. Instead, we attempted to use water as the liquid. We were able to get some results using water, but the simulations ran significantly slower and had difficulty obtaining any significant Atwood number change in the liquid phase as water would quickly evaporate before the density changed. Because of this, we created our own “numerical experiment" by using ideal

gases instead of liquids. This allowed us to obtain more realistic Atwood number changes that would drive the RTI. The two gases selected were air and Neon. These were chosen because the ratio of their gas constants R were such that the temperature gradient between the two fluids was minimized assuming pressure equilibrium at the interface and a negative initial Atwood number of $A_{t0} = -0.15$. The temperature ratio is found through the ideal gas equation, i.e. $\rho_1/\rho_2 = R_2T_2/R_1T_1$.

2.7 Initial perturbation and boundary conditions

The initial perturbation is used to create the instability that grows due to misaligned buoyancy and pressure force. a single, double, quadruple, and multi-modal period sinusoidal wave is specified at the interface,

$$\eta = A\cos(Bx + C). \tag{22}$$

where $A = 0.25$ cm, $B = 2\pi k/(x_{max} - x_{min})$, and $C = 0$. The wavenumber k was changed to increase/decrease the number of perturbations, and a multi-modal perturbation was achieved by overlaying a second perturbation of the same form but different wavenumber. This interface is stable at the start due to zero density gradient between the two fluids, but becomes unstable and grows as the density of the bottom fluid decreases and it's volume increases. The domain was initialized such that there was more of the top fluid than the bottom fluid, such that as the bottom expands, it does not push the interface into the top boundary. Reflective wall boundary conditions are used for all sides. Reflective B.C. are automatically assumed in xRage.

The size of the domain and height of the interface are sized such that an adequate Atwood number is reached before the interface reaches the top of the domain. More details on computing these dimensions is given in the Navier-Stokes solver section.

3 Stability theory and scaling analysis

Stability theory provides rough estimates of the early-time growth rates of the initial perturbation. The growth rates are obtained by working with momentum and continuity equations but are only valid before the onset of turbulence. This may prove to be more extendable to immiscible fluids as turbulence occurs much later. This section derives the growth rate for VED-driven RTI and compares the results to classical RTI growth rate estimates.

3.1 Linear stability theory for traditional RTI

We begin with a review of traditional stability theory for early-time (thus linear) classical RTI, and derive the growth rate. This section follows closely the work by Waddell et al. [14]. Linear stability theory for this problem considers two incompressible fluids having densities ρ_1, ρ_2 and velocity potentials ϕ_1, ϕ_2. Suppose these two fluids are separated by a perturbed planar interface with perturbation η. A sinusoidal perturbation is used to form the interface,

$$\eta = \eta_0 e^{ikx+\gamma t}, \tag{23}$$

where the perturbation grows exponentially in time at rate γ, with spatial wavenumber k. Through incompressibility, we seek the velocity potential for each material $\phi_{1,2}(x, z, t)$, where

$$u_i = \frac{\partial \phi}{\partial x_i} \quad \text{and} \frac{\partial^2 \phi}{\partial x_i^2} = 0 \quad \text{(incompressibility)}$$

The elementary solution for the velocity potential is found using the separable ansatz and the form of the initial perturbation

$$\phi_i(x, z, t) = \Phi_i(z) e^{ikx+\gamma t}$$

Where $\Phi_i(z)$ is the z-dependent velocity potential. From Laplace's equation $\partial^2\phi/\partial x_i^2 = 0$, we get:

$$\frac{d^2\Phi_i}{dz^2} - k^2\Phi_i = 0 \quad \Rightarrow \quad \Phi_i(z) = A_i e^{\mp kz}$$

The top fluid ($z > 0$) $\phi_1 \sim e^{-kz}$ decays upward while the the bottom fluid ($z < 0$): $\phi_2 \sim e^{kz}$ decays downward. Now we apply boundary conditions at the interface $z = 0$. The kinematic boundary condition (interface moves with the fluid) enforces

$$\frac{\partial \eta}{\partial t} = w_i = \frac{\partial \phi_i}{\partial z} \quad \text{at } z = 0.$$

Using $\eta \sim e^{\gamma t}$, and matching vertical velocity:

$$\gamma\eta = \left.\frac{\partial \phi_i}{\partial z}\right|_{z=0} \quad \Rightarrow \quad \frac{\partial \phi_1}{\partial z} = \frac{\partial \phi_2}{\partial z} = \gamma\eta$$

Next, the dynamic boundary condition due to pressure continuity across the interface is applied. From the linearized Bernoulli equation:

$$\frac{\partial \phi_i}{\partial t} = -\frac{p_i'}{\rho_i} - g\eta \Rightarrow p_i' = -\rho_i \left(\frac{\partial \phi_i}{\partial t} + g\eta\right)$$

Apply pressure continuity (it's not a shock):

$$p_1' = p_2' \quad \Rightarrow \quad -\rho_1(\gamma\phi_1 + g\eta) = -\rho_2(\gamma\phi_2 + g\eta)$$

Substitute $\phi_i = \Phi_i(0)e^{ikx+\gamma t}$, and relate $\Phi_i(0)$ to η using the kinematic condition:

$$\frac{\partial \phi_1}{\partial z} = -k\Phi_1(0) = \gamma\eta \Rightarrow \Phi_1(0) = -\frac{\gamma\eta}{k}$$

$$\frac{\partial \phi_2}{\partial z} = +k\Phi_2(0) = \gamma\eta \Rightarrow \Phi_2(0) = \frac{\gamma\eta}{k}$$

Now plug back into the dynamic condition:

$$-\rho_1\left(\gamma\left(-\frac{\gamma\eta}{k}\right) + g\eta\right) = -\rho_2\left(\gamma\left(\frac{\gamma\eta}{k}\right) + g\eta\right)$$

Simplify:

$$\rho_1\left(\frac{\gamma^2}{k}\eta - g\eta\right) = \rho_2\left(\frac{\gamma^2}{k}\eta + g\eta\right)$$

Now solve for γ^2:

$$(\rho_1 + \rho_2)\frac{\gamma^2}{k} = g(\rho_2 - \rho_1) \quad \Rightarrow \quad \gamma^2 = \frac{gk(\rho_2 - \rho_1)}{\rho_2 + \rho_1}$$

Thus we obtain the classical relationship with the Atwood number A_t

$$\gamma = \sqrt{kA_t g} \tag{24}$$

3.2 Linear stability theory for VED-driven RTI

The fundamental change in a VED-driven RTI is that the fluid densities are now functions of time $\rho_1(t), \rho_2(t)$, surface tension may be non-negligible (immiscible), and heat conduction between surfaces introduces thermal diffusion effects. The heating and subsequent expansion of the fluid also pushes up the interface and thus induces a local velocity change in the fluids, artificially varying the acceleration field. We derive solutions for immiscible fluids and assume uniform heating such that the densities are homogeneous in each material (Atwood number changes in time). The perturbation now depends on it's time history,

$$\eta = \eta_0 e^{ikx + \int_0^t \gamma(t)dt}$$

where the growth rate $\gamma(t)$ is a function of time now. The analysis is essentially the same if the timescale of the density changes are longer than $\gamma(t)^{-1}$

$$\gamma(t) = \sqrt{kA_t(t)g} \tag{25}$$

Adding the effects of surface tension and heat conduction make this considerably more difficult. Surface tension modifies the dynamic boundary condition at the interface by resisting curvature and introducing a pressure jump,

$$p_1' - p_2' = -\sigma k^2 \eta$$

where σ is the surface tension coefficient. This is added to the Bernoulli equation and gives the addition to the growth rate as

$$\gamma(t)^2 = kA_t(t)g - \frac{\sigma k^3}{\rho_1(t) + \rho_2(t)} \tag{26}$$

Finally, we consider heat conduction effects. Heat conduction introduces a localized density gradient in either fluid ($\rho(T) \approx \rho_0[1 - \alpha(T - T_0)]$). The Rayleigh-Bénard instability is triggered in each material because of this. Energy is governed by the heat diffusion equation:

$$\frac{\partial T}{\partial t} = \kappa_T \nabla^2 T$$

(Here $\kappa_T = \frac{k_T}{\rho c_p}$ is thermal diffusivity.) The key idea is that thermal diffusion tends to smooth temperature (and hence density) gradients, weakening buoyancy. In a linear analysis, this leads to a stabilizing term that scales like k^2. This is analogous to the thermal damping term in other buoyancy-driven instabilities like the Rayleigh–Bénard instability. The simplest model of this effect is to treat thermal diffusion as a damping term in the dispersion relation:

$$\gamma^2(t) = A(t)gk - \frac{\sigma}{\rho_1(t) + \rho_2(t)}k^3 - D_T(t)k^2 \tag{27}$$

Where $D_T \sim \frac{\Delta T \alpha g}{\kappa_T}$ encapsulates the effect of heat diffusion (details depend on system geometry and boundary conditions). This term appears naturally in more advanced stability analyses that couple the Navier–Stokes and energy equations using the Boussinesq approximation [3].

3.3 Scaling Analysis

In this section, we perform scaling anaylsis to determine if the VED-driven RTI or RBC is more dominant in the experiment by Root et al. [11]. The impact of neglecting viscosity is difficult to quantify since we do not have access to a true Navier-Stokes solver. It is believed that, at least in the experiments, the main driving force for the instability is actually convection due to temperature differentials, following the dynamics of Rayleigh-Bénard convection. This kind of convection and heat conduction is dependent on thermal boundary-layers, which is coupled with fluid boundary layers that require viscosity terms to properly simulate. RBC is typically quantified with the Rayleigh number,

$$R_a = \frac{g\beta\Delta T h^3}{\alpha\nu} \tag{28}$$

where α is the thermal diffusivity, β the thermal expansion coefficient, and h is the height of the fluid. The critical value at which RBC begins is $R_a \approx 1708$ [5]. Considering the top fluid, soybean oil, we must determine the characteristic length of the temperature gradient in the fluid. Through a 1D thermal simulation, Root et al. [11] determined that the maximum thermal boundary layer height was $h = 0.01m$. We use this approximation for the Rayleigh number computation, as well as the predicted maximum temperature difference $\Delta T = 363K$ estimated from an unpublished but similar experiment, shown in figure 3-2. For soybean oil the following coefficients are used: $\beta \approx 7 \times 10^{-4} K^{-1}$, $\alpha \approx 7 \times 10^{-8} m^2/s$ $\nu = 4.5 \times 10^{-5} m^2/s$ at $25°C$ This gives a Rayleigh number of $R_a = 7.9 \times 10^5$. From this basic evaluation, it is clear that not only is RBC present, it is significant. This contradicts the evaluation by Root et al. [11]. We believe the authors did not fully consider the effects of the temperature differential from the uneven heating of the fluid. An unpublished report that replicated the experiment by Root et al. [11] measured the Atwood number and found a maximum of $A_t \approx 0.006$, which is a very small compared to the effects of RBC as quantified by the non-dimensional analysis, So not only is RBC dominant in this case, it is also likely that a fluid boundary layer forms from the convection currents which further changes the heat conduction. In other words, viscosity is intrinsically coupled to RBC and both these quantities have a large impact on the evolution of the instability we are trying to study.

Stability theory and scaling analysis

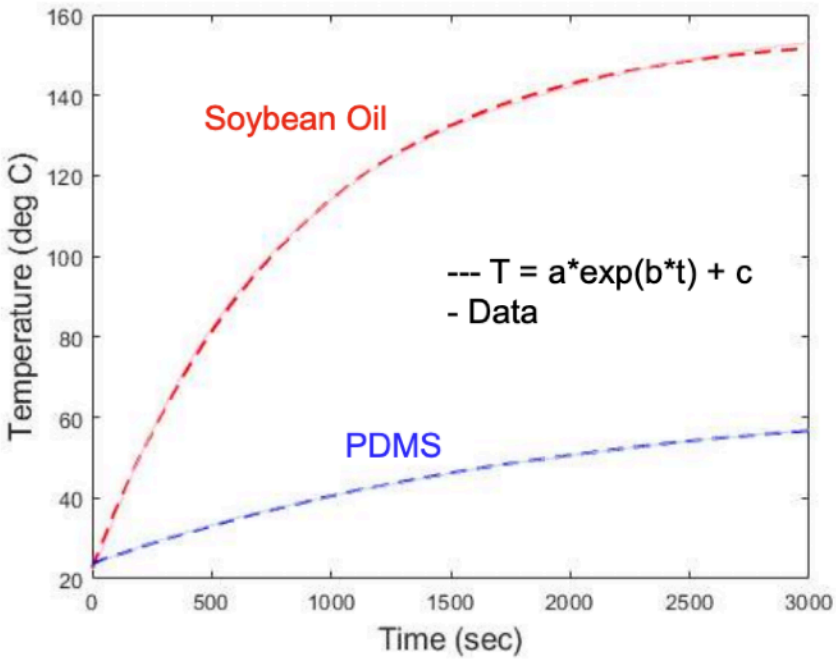

Figure 3-1: Experimentally measured temperature difference from VED-driven RTI experiment[1]

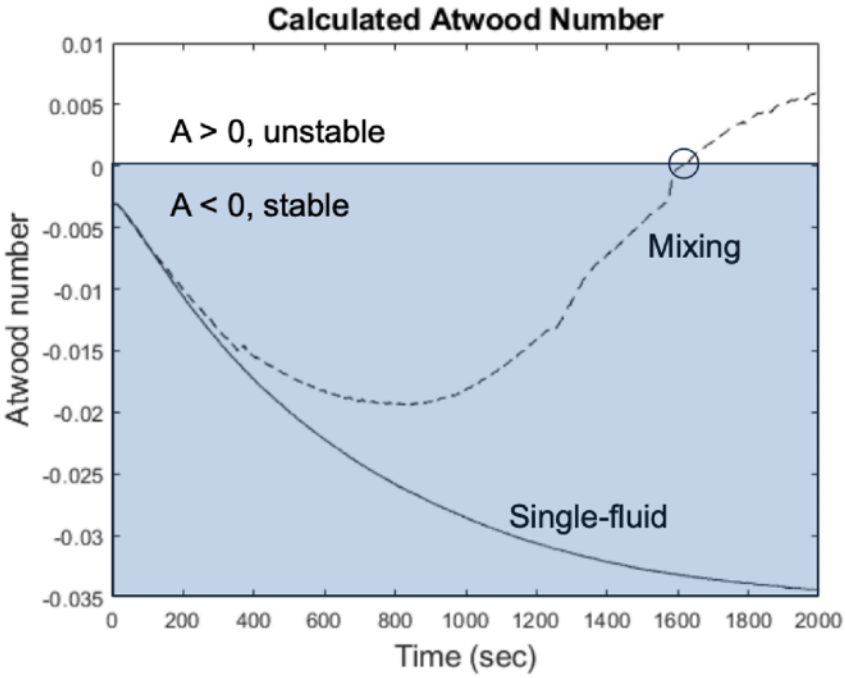

Figure 3-2: Experimentally measured Atwood number from VED-driven RTI experiment[1]

4 Navier-Stokes solver

From the scaling analysis, it is clear that viscosity is important for modeling RBC. This is not achievable with the Euler equations. In addition, simulating mixing correctly requires high-order, high-resolution simulations to capture all pertinent scales. This provides motivation to create a Navier-Stokes solver or direct numerical simulation (DNS). This section reviews the pertinent governing equations for a compressible fluid, and describes how the equations are solved for in a finite-difference code. The primitive variables are identified and are closed via physical approximations. To simplify things, we consider two miscible fluids only such that full multi-material tracking is not required and the interface is smooth.

4.1 Governing equations

The Navier-Stokes equations are the governing equations we must solve for. The continuity, momentum, and energy, and species transport equations are

$$\frac{\partial \rho}{\partial t} + \frac{\partial (\rho u_j)}{\partial x_j} = 0, \tag{29}$$

$$\frac{\partial (\rho u_i)}{\partial t} + \frac{\partial}{\partial x_j}(\rho u_i u_j + p\delta_{ij} - \tau_{ij}) = \rho g_i, \tag{30}$$

$$\frac{\partial (\rho E)}{\partial t} + \frac{\partial}{\partial x_j}\left[u_j(\rho E + p) - u_i \tau_{ij} + q_j\right] = \rho g_i u_i + S_E. \tag{31}$$

$$\frac{\partial (\rho Y)}{\partial t} + \frac{\partial (\rho u_j Y)}{\partial x_j} = \frac{\partial}{\partial x_j}\left(\rho D \frac{\partial Y}{\partial x_j}\right) \tag{32}$$

where ρ is the density, u_i is the velocity vector, p is pressure, e is specific internal energy,$E = e + \frac{1}{2}u_i u_i$ is the specific total energy, Y is the mass fraction of one of the fluids, D is the mass diffusivity ($D \approx 6.5 \times 10^{-5}$ for Neon in air), τ_{ij} is the viscous stress tensor, q_i is heat flux, g_i is the gravitational acceleration vector, and S_E is the energy source term. Now the constitutive relations are given. We assume a Newtonian fluid such that the viscous stress tensor is

$$\tau_{ij} = \mu\left(\frac{\partial u_i}{\partial x_j} + \frac{\partial u_j}{\partial x_i} - \frac{2}{3}\delta_{ij}\frac{\partial u_k}{\partial x_k}\right). \tag{33}$$

μ is the dynamic viscosity. For heat flux modeling, we use Fourier's law with enthalpy transport due to diffusion of two materials

$$q_i = -\kappa \frac{\partial T}{\partial x_i} + \rho D \frac{\partial h}{\partial Y}\frac{\partial Y}{\partial x_i} \tag{34}$$

κ is the thermal conductivity and T is temperature, h is the enthalpy (for two materials, $dh/dY = h_1 - h_2$). Next, Sutherland's Law is used to compute the dynamic viscosity of each material (denoted by the m subscript),

$$\mu_m(T) = \mu_{m,\text{ref}}\left(\frac{T}{T_{m,\text{ref}}}\right)^{3/2} \cdot \frac{T_{m,\text{ref}} + S_m}{T + S_m} \tag{35}$$

The thermal conductivity is easily found with the Eucken relation once dynamic viscosity is known,

$$\kappa_m = \frac{c_{p,m}\mu_m}{P_{r,m}} \tag{36}$$

where P_r is the Prandtl number (0.71 for air, 0.67 for Helium, etc.) and c_p is the specific heat at constant pressure (c_v for constant volume). For simplicity, we assume that c_p, c_v are constants. They allow us to relate total specific energy to temperature,

$$e = c_v T,\ h = c_p T \tag{37}$$

Next, ideal gas equation of state is used to relate thermodynamic properties

$$p = \rho R T \tag{38}$$

with R the specific gas constant in the current cell. Finally, we now identify the primitive variables for which we must evolve in time. The primitive variables we select to evolve are the density ρ, velocity vector u_i, total specific energy E, and mass fraction Y. These are the four natural primitive variables that the Navier-Stokes equations evolves. These primitive variables are all that are required to compute secondary variables, like temperature $T = \frac{1}{c_v}\left(E - \frac{1}{2}u_k u_k\right)$, dynamic viscosity, etc.

4.2 Mixing rules

For different materials, the dynamic viscosity, thermal conductivity, microscopic density, and all material constants (c_p, c_v, R) are different and depends on the mass fraction i.e. $\mu(Y), \kappa(Y)$. For simplicity, we will assume that D is constant and the same for both materials. Material constants are also different for each material. The mixing rules govern how the average of these quantities in the discrete cell is computed. The two options are the simple linear mix rule,

$$a = Y a_1 + (1 - Y) a_2, \tag{39}$$

where a is the variable of interest (κ, μ, etc.), or Wilke's mixing rule,

$$a = \frac{a_1 Y}{Y + \phi_{12}(1 - Y)} + \frac{a_2(1 - Y)}{1 - Y + \phi_{21} Y}; \tag{40}$$

with the tensor

$$\phi_{ij} = \frac{\left[1 + \left(\frac{a_i}{a_j}\right)^{1/2}\left(\frac{M_j}{M_i}\right)^{1/4}\right]^2}{\sqrt{8\left(1 + \frac{M_i}{M_j}\right)}} \tag{41}$$

where M_i is the molar mass of the specific material $M_{\text{air}} \approx 0.029$ kg/mol, $M_{\text{He}} \approx 0.004$ kg/mol, etc).

4.3 Heat source

To study variable Atwood-number RTI, we have added a preferential heat source to the energy equation S_E. This heat source is designed to heat up one fluid faster than the other, and thus depends on the mass fraction. The simplest model has the form

$$S_E(Y) = \rho Q_0 (1 - Y) \tag{42}$$

where Q_0 is the peak heating rate $[W/kg]$ and $f(Y)$ is a weighting function. A few options exist for the weighting function. The easiest is binary switching,

$$f(Y) = \begin{cases} 1, & \text{if } Y > 0.5 \\ 0, & \text{otherwise} \end{cases} \tag{43}$$

a smooth weighting function can also be used,

$$f(Y) = Y \quad \text{or} \quad f(Y) = \frac{1}{2}(1 + \tanh(k(Y - 0.5))) \tag{44}$$

or a spatially localized form such as

$$f(x, Y) = Y \cdot \exp\left(-\frac{(x - x_c)^2}{\sigma^2}\right) \tag{45}$$

This way, one fluid (say, species 1) heats up faster, expanding and reducing in density over time — altering the local Atwood number. Numerical methods for solving all the equations presented are detailed in the appendix.

4.4 Stability and scale requirements

For explicit time schemes, time step is limited by both acoustic and advective waves. The acoustic time scale $\Delta x/c$ is often the most restrictive in compressible DNS. Stiff diffusion (binary mixture), may also be limiting. The CFL condition is

$$\Delta t \leq \min\left(\frac{C_{\text{adv}}\Delta x}{|u| + c}, \frac{C_{\text{visc}}\Delta x^2}{\nu}, \frac{C_{\text{diff}}\Delta x^2}{D}\right) \tag{46}$$

where c is the local speed of sound, Δx is the grid spacing and $C_{\text{adv}}, C_{\text{visc}}, C_{\text{diff}} \sim 0.2$–$0.5$ are the CFL numbers. To fully resolve turbulence in DNS, the smallest dynamically important scales must be resolved by the grid. The scales of interests are the Kolmogorov scale η for viscous dissipation,

$$\eta = \left(\frac{\nu^3}{\epsilon}\right)^{1/4}$$

with ϵ the local dissipation rate and $\Delta x \leq \eta$ (or $\Delta x/\eta \leq 1$), and the Batchelor scale η_B: for scalar (species) dissipation

$$\eta_B = \eta/\sqrt{Sc} \quad (\text{for } Sc > 1)$$

where $Sc = \nu/D$ is the Schmidt number. So, if $Sc \gg 1$ (e.g., heavy gases in air), then one needs finer resolution to resolve scalar gradients than velocity gradients.

Therefore,to resolve all relevant turbulent scales, we must satisfy:$\Delta x \leq \eta$ $\Delta x \leq \eta_B$ (if $Sc > 1$). The mesh size estimate in 3D is

$$N_x N_y N_z \sim \left(\frac{L}{\eta}\right)^3 \sim Re^{9/4}$$

L is the domain size, and Re is the large-scale Reynolds number. So a moderate DNS at $Re_\lambda = 100$ may already require 512^3–1024^3 grid points.

While not strictly necessary for this project, it is important to keep in mind that thermodynamic and diffusive phenomena may require their own resolution scales: viscous and thermal boundary layers (especially near walls), acoustic scales to ensure $\Delta x \ll \lambda_{\min}$ for any relevant acoustic waves, and shock thickness in high Mach flows. Compressibility and species transport may also imply steep gradients in density, temperature, species mass fraction, which require fine resolution, especially at interfaces or reaction zones.

4.5 Initialization

High-fidelity initialization helped to inform both the DNS and Euler-solver initial conditions. The six primitive variables must be initialized to run the simulation. We are looking to simulate a VED-driven RTI, so to initialize such a simulation, we need a thermodynamically consistent and hydrostatically balanced state, with small perturbations to seed the instability. We take the two species to be gases (e.g., air and Neon), gravity in the vertical z-direction, and a heated lower layer. We set a smooth transition between the two fluids to avoid sharp gradients,

$$Y(z) = \frac{1}{2}\left[1 + \tanh\left(\frac{z - z_0}{\delta}\right)\right] \tag{47}$$

where z_0 is the interface location and δ is the interface thickness. Note that $Y = 0$ is the heavier fluid (e.g., air) and $Y = 1$ is the lighter fluid (e.g., Neon). We then perturb the interface by super-imposing a sinusoidal perturbation field in the mixing-layer of Y. A very fine perturbation with random waves is shown in the density profile in figure 4-1. Next, the equation of state (equation 38) is used along with hydrostatic equilibrium $\frac{dp}{dz} = -\rho g$ to find density and pressure. By prescribing a density profile $\rho(z)$, we can integrate the hydrostatic equation numerically and obtain the relationship where the pressure at the bottom $p(z_0)$ is known.

$$p_{(i+1)} = p_{(i)} - \rho_{(i)} g \Delta z \tag{48}$$

Finally, all velocity components are set to zero everywhere and total specific energy is easily computed using $E = e + \frac{1}{2}u_i u_i$ and equation 37.

There are two strategies to simulating variable-Atwood number RTI: expansion of the bottom fluid and pushing out the top fluid through a constant pressure outflow such that only the bottom fluid changes (reduces) in density, or a constant-volume approach where the bottom fluid expands in volume and the top fluid contracts. The second is simpler and will give a larger final Atwood number due to the compression/expansion of both fluids. It will also require a smaller domain and we don't have to worry about the fluids being pushed out. We now present the way the domain physical size is computed such that a desired Atwood number is obtained with a certain grid discretization. To give ourselves a fighting chance, we will try to limit the number of grid points in the finest direct, the vertical z-direction, to 4096 points. We will also limit the change in Atwood number from 0.03 to 0.06. How much heating is needed? We assume constant pressure at interface (hydrostatic equilibrium) and no heat transfer between the fluids. The cross-sectional area stays constant along with total height,

$$L_z = h_{b0} + h_{t0},\ m_b = \rho_{b0} A h_{b0},\ m_t = \rho_{t0} A h_{t0}$$

via pressure continuity at the interface, we get that $\rho_b T_b = \rho_t T_t$. By combining with mass conservation we get and rewriting in terms of Atwood number, we get

$$h_b = \frac{m_b T_b}{m_b T_b + m_t T_t} L_z = L_z \frac{\rho_{b0} h_{b0} \frac{1+A_t}{1-A_t}}{\rho_{t0} h_{t0} + \rho_{b0} h_{b0} \frac{1+A_t}{1-A_t}} = L_z f(A_t)$$

This shows that the height of the bottom fluid will always be a fraction ($f(A_t)$) of the total height. We can constrain this problem by enforcing a minimum top-fluid height. We enforce that $h_t = h_{b0}$, such that the domain height must satisfy

$$L_z \geq \frac{h_t}{1 - f(A_t)}$$

Now we compute the Reynolds number we expect to see. We use the characteristic buoyancy velocity scale which assumes that the RTI length reaches the initial height of the bottom fluid, $U \sim \sqrt{A_t g h_{b0}}$. Turbulent dissipation is approximated by $\epsilon \sim U^3/h_{b0}$ which, when dynamic viscosity is known, gives us the Kolmogorov scale $\eta = (\nu^3/\epsilon)^{1/4}$ for which the grid must be smaller. The same check is done for the Batchelor scale $\eta_B = \eta/\sqrt{\nu/D}$. Thus we get the final relation,

$$\frac{h_t}{1 - f(A_t)} \leq L_z \leq \min(N_z\eta, N_z\eta_B),\ L_x \leq \min(N_x\eta, N_x\eta_B),\ L_y \leq \min(N_y\eta, N_y\eta_B) \tag{49}$$

Thus we specify A_t, h_{b0}, L_z, and N_z to fully constrain the problem

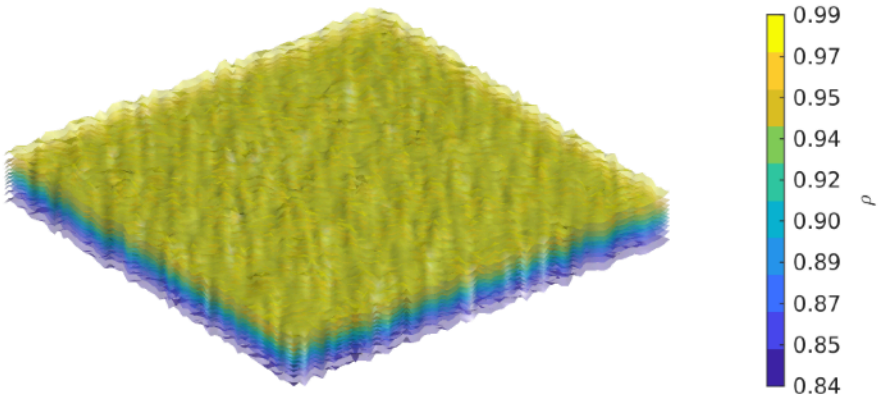

Figure 4-1: Initial density interface field using random perturbations.

5 Results

Results are given for initial growth of VED-driven RTI using xRage. The results are 2D and are given for four different kinds of perturbations; a single, two-period, four-period, and multi-modal period. By holding all of properties of the mixture identical besides the wave number, the affect that perturbation frequency has on the growth of the perturbation can be studied.

5.1 Single-mode perturbations

Figure 5-1 shows the initial density fields for three perturbation types. All perturbation heights were set to 0.25 cm. Both fluids have uniform pressure and temperature fields, set to 101,325 Pa and 293.15 K, respectively. During the stable period, a few key events happen: the center of the perturbation descends and reverses its direction, the perturbation contracts but retains its shape, and the perturbation dissipates due to surface tension and heat conduction, leading to delayed growth. Figure 5-2 shows that the densities of both fluids at 0.5 seconds are approximately equal due to energy deposition from an internal source into the lower fluid, resulting in an Atwood number of zero. Initial perturbation amplitude decays while still in the stable configuration. Figure 5-3 shows the point when the density gradient has reversed relative to the initial condition, resulting in a positive Atwood number.

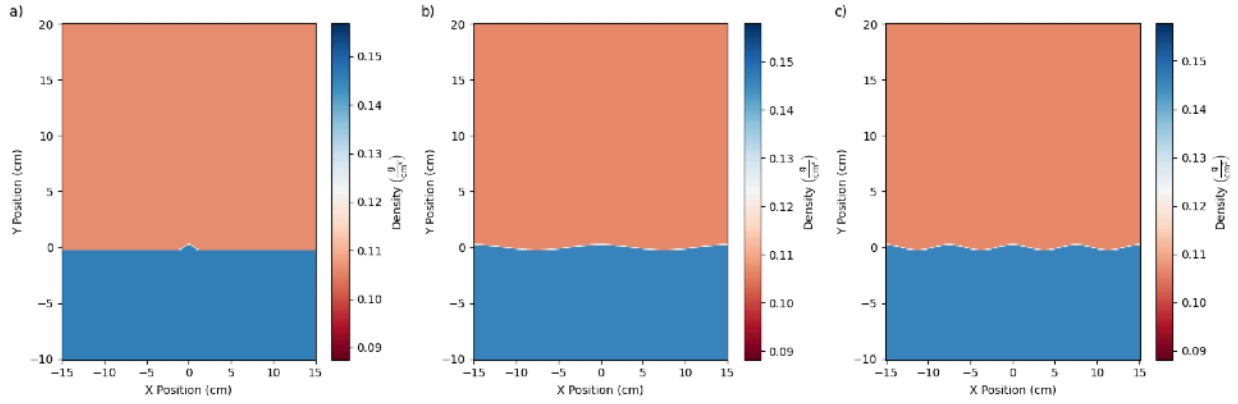

Figure 5-1: Initial density fields for three perturbation types: a) a single period perturbation; b) two-period perturbation; c) four-period perturbation.

Diffusive effects play a significant role in the final evolution of each perturbation configuration. Higher wavenumber perturbations are also more susceptible to damping during periods when the Atwood number is negative (stable). Additionally, physical mechanisms such as heat diffusion and surface tension contribute further to the suppression of higher-frequency perturbations. These diffusive effects can alter both the amplitude and the shape of the perturbation, creating multi modal shapes. Changing only the amplitude of the perturbation does not affect the growth rate, rather increasing the time required to reach a certain height. In the case of the four-period perturbation—shown in Figures 5-1 to 5-5c, the initial disturbance is damped so significantly that the interface effectively flattens out before any meaningful growth can occur. As a result, the instability develops much slower compared to configurations with fewer initial wavelengths. The single and two-period cases have a similar growth qualitatively.

Results

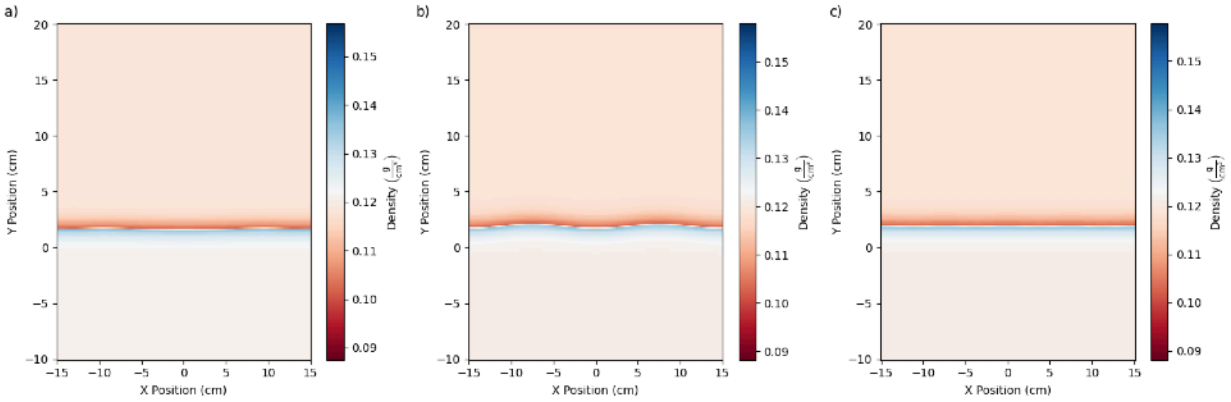

Figure 5-2: Density fields of three perturbations types at 0.5 seconds for a) single perturbation, b) two-period perturbation, and c) four-period perturbation.

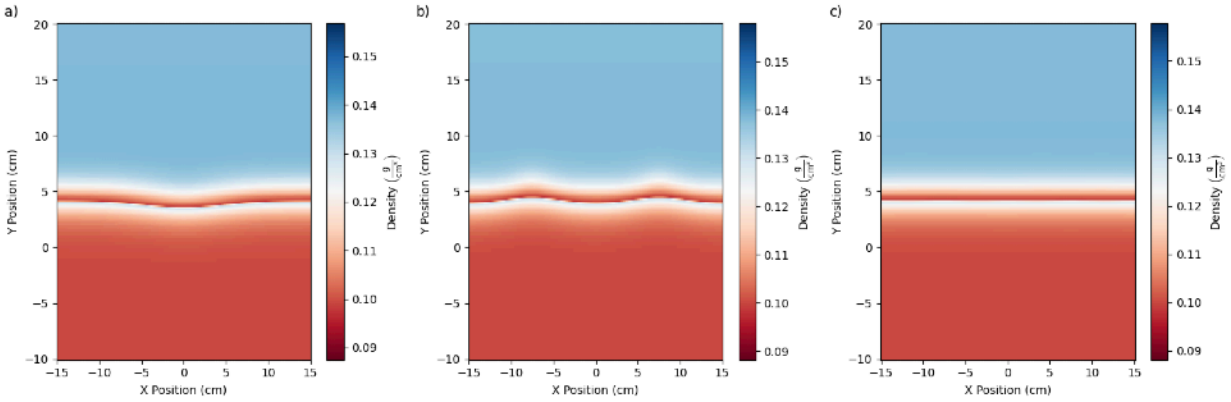

Figure 5-3: Density fields of three perturbations types at 1.3 seconds for a) single perturbation, b) two-period perturbation, and c) four-period perturbation.

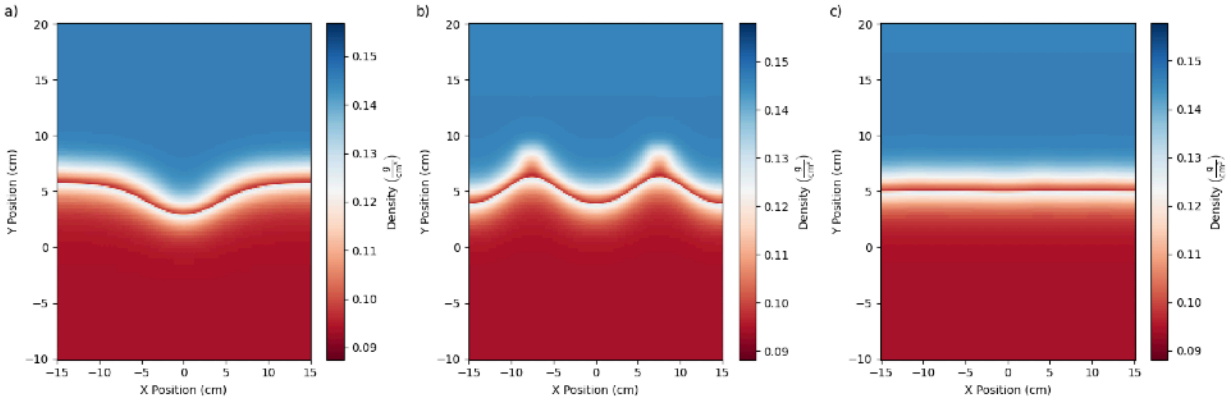

Figure 5-4: Density fields of three perturbations types at 1.65 seconds for a) single perturbation, b) two-period perturbation, and c) four-period perturbation.

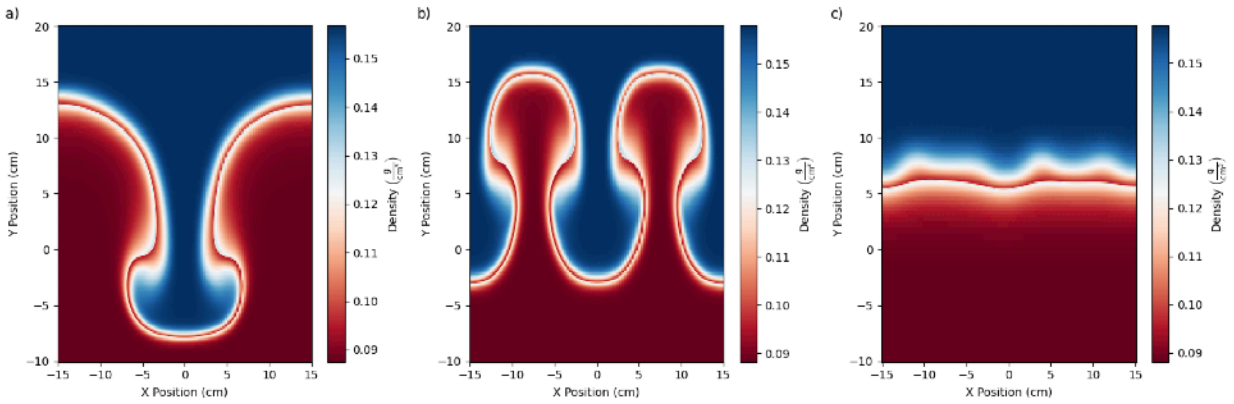

Figure 5-5: Density fields of three perturbations types at 2.13 seconds for a) single perturbation, b) two-period perturbation, and c) four-period perturbation.

5.2 Growth rates and Atwood number

The growth rate and Atwood can be measured in the xRage simulations. Figure 5-6 shows the evolution of the Atwood numbers for the three single-wavenumber cases. The Eulerian simulations follow relatively closely to the simplified Atwood number evolution model (blue line), and thus shows that the method for predicting Atwood number beforehand is sufficient for domain sizing as long as conservative bounds are used. All three cases have nearly the same Atwood number evolution except at later times where mixing becomes more prominent and heat conduction begins to dissipate heat and diffuses the density gradients. The drop in the two-period case corroborates the visual results, where there is more surface area between the fluids (due to more instability growths) and thus greater effective heat transfer. Figure 5-7 provides a comparison of perturbation

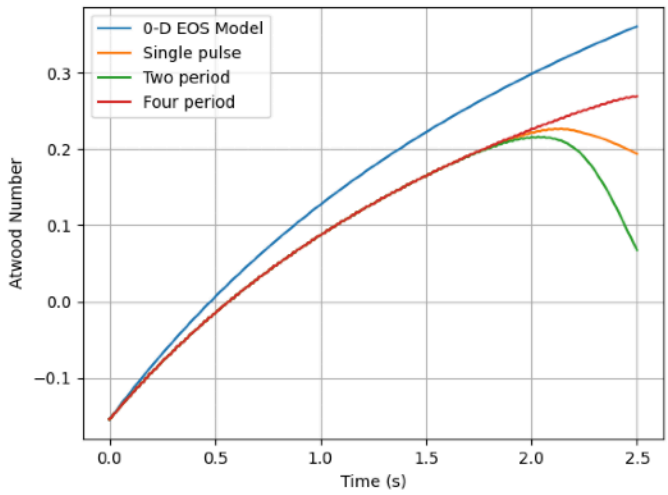

Figure 5-6: Simulation Atwood number evolution in time compared to zero dimensional model derived from equation of state.

amplitude growth from simulations and theoretical predictions for both traditional and VED-driven

RTI. The theoretical prediction for VED-driven RTI does not include the heat diffusion dampening term because an exact form for this was not determined, but it does include dampening from surface tension. The classical RTI height growth is started at 0.5 seconds when the VED-driven RTI becomes unstable for a fairer comparison. Perturbation heights are measured in simulations for all three single-wavenumber cases up to 0.5 seconds of evolution. The traditional RTI model assumes a constant Atwood number of 0.25. Delayed and lowered growth rates are observed for all cases compared to traditional RTI. This matches with what is predicted from linear stability theory. The height evolution from the simulation compared to the VED-driven RTI theory also agree for early-time behavior and have similar slopes past 1.7 seconds, except for the four-period case. The height of the four-period cases is almost 3 times as high as the height predicted by theory. This is counter-intuitive and shows signs that additional dynamics not accounted for are impacting the four-period case. One of these can be the RBC, where if the convection cells form in a favorable way, can increase growth rate. This is not captured in the linear stability theory.

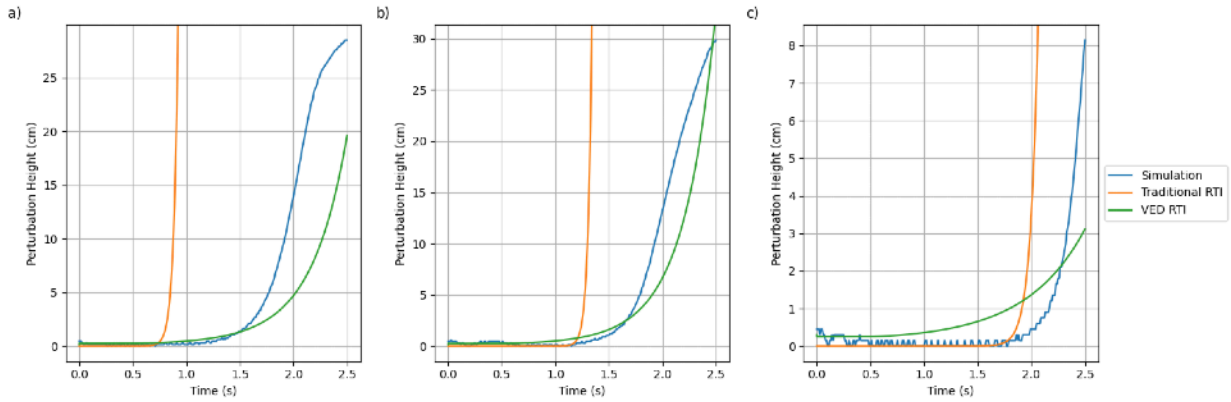

Figure 5-7: Comparison of perturbation amplitude growth from simulations and theoretical predictions for both traditional and VED-driven RTI (ignoring heat diffusion) for a) a single-period perturbation, b) a two-period perturbation, and c) a four-period perturbation.

5.3 Multi-modal perturbation

The multi-modal perturbation explores the growth rate and interaction of different-sized perturbations. The initial Atwood number is reduced to $A_{t0} = -0.004$ and is left to grow up to $A_t = 0.4$. However, later time behavior is likely under-resolved due to the rapid structure-breakdown exacerbated by secondary instabilities/interactions due to shearing. Two sinusoidal wave perturbations at double the wavenumber ratio i.e. $k_1 = 2k_2$ are superimposed. This gives three large peaks and two smaller peaks in between, as seen in figure 5-8 a. The higher wavenumber perturbations grow faster, as expected from classical RTI linear stability theory. Dampening effects of surface tension and heat diffusion were not as pronounced, and follow similar growth to the two-wave perturbation. It is seen that the smaller wavenumber bubbles interfere with the root of the larger bubbles, and a shearing effect disconnects the top “mushroom cloud" of the larger perturbations and begins forming secondary instabilities on the lower half, as seen in figure 5-8 c-d.

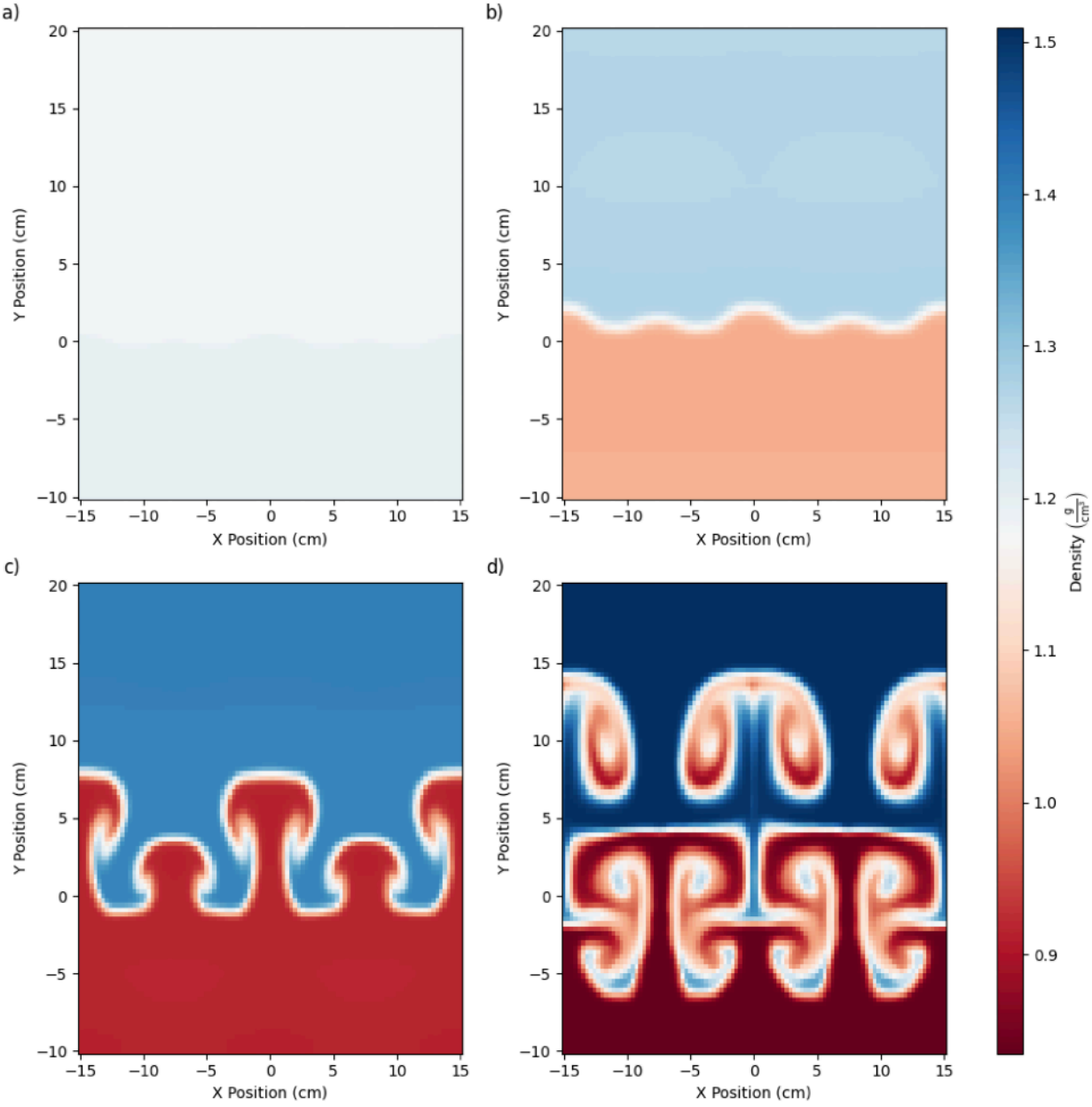

Figure 5-8: Multi Modal simulation: a) Initial conditions; b) 0.3 seconds; c) 0.75 seconds; and d) 1.15 seconds

6 Conclusion

In this work, we have presented the key dynamics to VED-driven RTI and performed simulations to study the early-time behavior of this unique phenomenon. We have identified, via scaling analysis, that in past experiments, RBC was likely the driving mechanism and that the fluid selection added complexities that could not be captured fully with xRage, the Eulerian code. The main problem is the equation of state is not readily available and thus prevents fair direct comparison with simulations and experimental findings. Immiscibility, surface tension, and heat conduction were found to have diffusive behavior on the VED-driven RTI early-time growth rate. This was found via linear stability theory accounting for the additional effects. A GPU-based finite-difference DNS code was also created from scratch to simulate the VED-driven RTI governed by the Navier-Stokes. The motivation for this was to be able to capture viscous effects, such as RBC, and obtain accurate predictions for late-time, nonlinear behavior. Finally, 2D simulations were performed using xRage for various initial perturbations. These simulations explored how the perturbations (changing wavenumber and multi-modal) impacted the initial growth rate. Results were consistent with the linear stability theory, where increased wavenumber increased growth rate up to a point, where diffusive effects started becoming more prominent and decreased the growth rate. The time period where the Atwood number was still stable was also found to dampen/flatten the initial perturbation which meant that the starting bubble height was reduced.

6.1 Future Work

Future work will mostly focus on studying late-time behavior of VED-driven RTI. We hope to be able to explore nonlinear growth, mixing, and transition to turbulence. The most significant step towards this is completing of the DNS code. We were unable to obtain any presentable results with the DNS code due to several issues: the multi-GPU framework was not implemented so we could only run under-resolved grids with sufficient memory on the single GPU, the implementation of the equations and numerical methods was not tested rigorously enough to give confidence in the results, and the simulation run-time, even for under-resolved grids, was too long and could not be completed in the given time frame. However, the code does run and outputs correct initialization. We hope to complete this code in the future.

Additional efforts should be focused on a more in-depth linear stability analysis to obtain more accurate growth rate laws. This would give further insight into the important early-time dynamics and can be compared against Eulerian simulations using xRage. Finally, the 2D simulations can also provide much more information than what was provided in this report. We can obtain quantitative data on growth rate and dampening of the initial perturbation, and try out various different initial conditions, Atwood number ranges, and types of fluids. Grid convergence studies should also be performed to ensure the simulations are not under-resolved.

Appendix A: Numerical methods for Navier-Stokes solver

This appendix describes the finite-difference numerical methods used for the direct numerical simulation of the Navier-Stokes equations.

A.1 Equation forms

It is well known that taking the derivative twice for double-derivative terms leads to instabilities, especially for viscous terms. Because of this, we decompose the diffusion terms and take the second derivatives directly. The equations can be written in the conservative form:

$$\frac{\partial \rho}{\partial t} = \underbrace{-\frac{\partial}{\partial x_1}(\rho u_1) - \frac{\partial}{\partial x_2}(\rho u_2) - \frac{\partial}{\partial x_3}(\rho u_3)}_{\text{flux}} \tag{50}$$

$$\frac{\partial \rho u_i}{\partial t} = \underbrace{-\frac{\partial}{\partial x_1}(\rho u_i u_1 + p\delta_{i1}) - \frac{\partial}{\partial x_2}(\rho u_i u_2 + p\delta_{i2}) - \frac{\partial}{\partial x_3}(\rho u_i u_3 + p\delta_{i3})}_{\text{flux}} \underbrace{\frac{\partial}{\partial x_1}(\tau_{i1}) + \frac{\partial}{\partial x_2}(\tau_{i2}) + \frac{\partial}{\partial x_3}(\tau_{i3})}_{\text{diffusion}} + \rho g_i \tag{51}$$

$$\frac{\partial \rho E}{\partial t} = \underbrace{-\frac{\partial}{\partial x_1}(u_1 \rho E + u_1 p) - \frac{\partial}{\partial x_2}(u_2 \rho E + u_2 p) - \frac{\partial}{\partial x_3}(u_3 \rho E + u_3 p)}_{\text{flux}} \underbrace{+\frac{\partial}{\partial x_1}(u_i \tau_{i1} - q_1) + \frac{\partial}{\partial x_2}(u_i \tau_{i2} - q_2) + \frac{\partial}{\partial x_3}(u_i \tau_{i3} - q_3)}_{\text{diffusion}} + \rho g_i u_i + S_E \tag{52}$$

$$\frac{\partial \rho Y}{\partial t} = \underbrace{-\frac{\partial}{\partial x_1}(\rho u_1 Y) - \frac{\partial}{\partial x_2}(\rho u_2 Y) - \frac{\partial}{\partial x_3}(\rho u_3 Y)}_{\text{flux}} + \underbrace{\frac{\partial}{\partial x_1}\left(\rho D \frac{\partial Y}{\partial x_1}\right) + \frac{\partial}{\partial x_2}\left(\rho D \frac{\partial Y}{\partial x_2}\right) + \frac{\partial}{\partial x_3}\left(\rho D \frac{\partial Y}{\partial x_3}\right)}_{\text{diffusion}} \tag{53}$$

Now, the respective diffusion terms can be decomposed into terms that can be fed into the flux computation (mixed-diffusion), double derivatives (pure diffusion) and source terms.

$$\begin{aligned}\text{Momentum diffusion} = &\underbrace{\frac{\partial}{\partial x_1}\left(\mu\frac{\partial u_1}{\partial x_i} - \mu\frac{2}{3}\delta_{i1}\frac{\partial u_{k\neq 1}}{\partial x_{k\neq 1}}\right)}_{\text{mixed-diffusion}} + \underbrace{\mu\frac{\partial^2 u_i}{\partial x_1^2} - \mu\frac{2}{3}\delta_{i1}\frac{\partial^2 u_1}{\partial x_1^2}}_{\text{pure diffusion}} + \underbrace{\frac{\partial \mu}{\partial x_1}\left(\frac{\partial u_i}{\partial x_1} - \frac{2}{3}\delta_{i1}\frac{\partial u_1}{\partial x_1}\right)}_{\text{source}} \\ &+ \underbrace{\frac{\partial}{\partial x_2}\left(\mu\frac{\partial u_2}{\partial x_i} - \mu\frac{2}{3}\delta_{i2}\frac{\partial u_{k\neq 2}}{\partial x_{k\neq 2}}\right)}_{\text{mixed-diffusion}} + \underbrace{\mu\frac{\partial^2 u_i}{\partial x_2^2} - \mu\frac{2}{3}\delta_{i2}\frac{\partial^2 u_2}{\partial x_2^2}}_{\text{pure diffusion}} + \underbrace{\frac{\partial \mu}{\partial x_2}\left(\frac{\partial u_i}{\partial x_2} - \frac{2}{3}\delta_{i2}\frac{\partial u_2}{\partial x_2}\right)}_{\text{source}} \\ &+ \underbrace{\frac{\partial}{\partial x_3}\left(\mu\frac{\partial u_3}{\partial x_i} - \mu\frac{2}{3}\delta_{i3}\frac{\partial u_{k\neq 3}}{\partial x_{k\neq 3}}\right)}_{\text{mixed-diffusion}} + \underbrace{\mu\frac{\partial^2 u_i}{\partial x_3^2} - \mu\frac{2}{3}\delta_{i3}\frac{\partial^2 u_3}{\partial x_3^2}}_{\text{pure diffusion}} + \underbrace{\frac{\partial \mu}{\partial x_3}\left(\frac{\partial u_i}{\partial x_3} - \frac{2}{3}\delta_{i3}\frac{\partial u_3}{\partial x_3}\right)}_{\text{source}}\end{aligned} \tag{54}$$

$$\begin{aligned}\text{Energy diffusion} = u_i \times (\text{momentum diffusion}) \\ &\underbrace{-\kappa\frac{\partial^2 T}{\partial x_1^2} + \rho D(c_{p,1} - c_{p,2})T\frac{\partial^2 Y}{\partial x_1^2}}_{\text{pure diffusion}} \underbrace{- \frac{\partial \kappa}{\partial x_1}\frac{\partial T}{\partial x_1} + \frac{\partial}{\partial x_1}\left(\rho D(c_{p,1} - c_{p,2})T\right)\frac{\partial Y}{\partial x_1}}_{\text{source}} \\ &\underbrace{-\kappa\frac{\partial^2 T}{\partial x_2^2} + \rho D(c_{p,1} - c_{p,2})T\frac{\partial^2 Y}{\partial x_2^2}}_{\text{pure diffusion}} \underbrace{- \frac{\partial \kappa}{\partial x_2}\frac{\partial T}{\partial x_2} + \frac{\partial}{\partial x_2}\left(\rho D(c_{p,1} - c_{p,2})T\right)\frac{\partial Y}{\partial x_2}}_{\text{source}} \\ &\underbrace{-\kappa\frac{\partial^2 T}{\partial x_3^2} + \rho D(c_{p,1} - c_{p,2})T\frac{\partial^2 Y}{\partial x_3^2}}_{\text{pure diffusion}} \underbrace{- \frac{\partial \kappa}{\partial x_3}\frac{\partial T}{\partial x_3} + \frac{\partial}{\partial x_3}\left(\rho D(c_{p,1} - c_{p,2})T\right)\frac{\partial Y}{\partial x_3}}_{\text{source}}\end{aligned} \tag{55}$$

$$\text{Species diffusion} = \underbrace{\rho D\frac{\partial^2 Y}{\partial x_1^2} + \rho D\frac{\partial^2 Y}{\partial x_2^2} + \rho D\frac{\partial^2 Y}{\partial x_3^2}}_{\text{pure diffusion}} + \underbrace{\frac{\partial \rho}{\partial x_1}D\frac{\partial Y}{\partial x_1} + \frac{\partial \rho}{\partial x_2}D\frac{\partial Y}{\partial x_2} + \frac{\partial \rho}{\partial x_3}D\frac{\partial Y}{\partial x_3}}_{\text{source}} \tag{56}$$

Note that all terms can be computed from conservative variables. for example, the temperature derivative is

$$\frac{\partial T}{\partial x_i} = \frac{1}{c_v}\left[\frac{1}{\rho}\left(\frac{\partial(\rho E)}{\partial x_i} - E\frac{\partial \rho}{\partial x_i}\right) - u_k\left(\frac{1}{\rho}\frac{\partial(\rho u_k)}{\partial x_i} - \frac{u_k}{\rho}\frac{\partial \rho}{\partial x_i}\right)\right] - \frac{T}{c_v}(c_{v1} - c_{v2})\left(\frac{1}{\rho}\left(\frac{\partial(\rho Y)}{\partial x_i} - Y\frac{\partial \rho}{\partial x_i}\right)\right)$$

or the velocity derivatives are

$$\frac{\partial u_i}{\partial x_j} = \left(\frac{\partial(\rho u_i)}{\partial x_j} - u_i\frac{\partial \rho}{\partial x_j}\right)/\rho$$

A.2 Spatial discretization

A finite-difference scheme is used to evaluate spatial derivatives. The finite difference approximation f_i' to the first derivative $\partial f(\boldsymbol{x}_i)/\partial x$ at the node i (varying in x-direction) with uniform grid spacing is evaluated by solving a tridiagonal system of the form [8]

$$\alpha f_{i-1}' + f_i' + \alpha f_{i+1}' = b\frac{f_{i+2} - f_{i-2}}{4h} + a\frac{f_{i+1} - f_{i-1}}{2h} \tag{57}$$

The relations between the coefficients a,b and a are derived by matching the Taylor series coefficients of various order. For example, with $a = 2(\alpha+2)/3,\ b = (4\alpha-1)/3$, a family of fourth order schemes is obtained. It may be noted that as $\alpha \to 0$ this family merges into the well known fourth order central difference scheme. Similarly for $\alpha = 1/4$ the classical Padé scheme is recovered and for $\alpha = 1/3$ the leading order truncation error coefficient vanishes and the scheme is formally sixth order accurate. The second derivatives are evaluated in a similar way,

$$\alpha f''_{i-1} + f''_i + \alpha f''_{i+1} = b\frac{f_{i+2} - 2f_i + f_{i-2}}{4h^2} + a\frac{f_{i+1} - df_i + f_{i-1}}{h^2} \tag{58}$$

with $a = 4(1-\alpha)/3,\ b = (10\alpha - 1)/3$. Again this approaches the classical fourth-order central difference as $\alpha \to 0$ and $\alpha = 1/10$ for Padé. When $\alpha = 2/11$, a sixth-order scheme is recovered. In this work, the sixth-order scheme is used. The spectral-like accuracy of the schemes follows from the nature of the dispersive errors associated with eq. 57. It has been shown that compared to the traditional finite difference schemes these schemes reduce the dispersive errors over a wider band of the length scales represented on the grid [8].

A.3 Temporal discretization

The minimum acceptable time integration order for DNS is typically fourth-order. Due to the time-resolving nature of the simulation, and explicit scheme is adequate. We implemented the Runge-Kutta fourth-order scheme (RK4)

$$\begin{aligned} k_1 &= \frac{\partial f(t^n)}{\partial t} \\ k_2 &= \frac{\partial (f(t^n) + \frac{\Delta t}{2}k_1)}{\partial t} \\ k_3 &= \frac{\partial (f(t^n) + \frac{\Delta t}{2}k_2)}{\partial t} \\ k_4 &= \frac{\partial (f(t^n) + \Delta t k_3)}{\partial t} \\ f^{n+1} &= f^n + \frac{\Delta t}{6}(k_1 + 2k_2 + 2k_3 + k_4) \end{aligned} \tag{59}$$

That's all there is to it!

A.4 Slip-wall boundary conditions

Slip walls are used to ensure constant-volume domain and are used and neglect frictional forces. if $i = n$ where n is the normal direction to the wall, then we impose zero normal velocity $u_i = 0$ and zero shear stress $\frac{du_{j\neq n}}{dx_i} = 0$. The wall is also adiabatic and non-reactive such that all scalar derivatives normal to the wall are zero, i.e. $\frac{dY}{dx_i} = 0$, $\frac{dT}{dx_i} = 0$, $\frac{dp}{dx_i} = 0$, etc. These conditions impose Dirichlet (state is zero) and Neumann (derivative of state is zero) numerical boundary conditions which are enforced through the matrix and RHS formation. Note that Neumann BC are enforced through ghost states for first derivative, while Dirichlet requires explicit state enforcement and single-sided stencils. Second-derivatives with Neumann conditions also require a biased stencil.

Appendix A: Numerical methods for Navier-Stokes solver

The Neumann and Dirichlet BC inform us how to form the tridiagonal matrix. We explicitly describe the numerical BC for flux and diffusion terms. For the flux terms,

$$-\frac{\partial}{\partial x_i}(\rho u_i) \rightarrow \text{Dirichlet}, \; -\frac{\partial}{\partial x_j}\left(\rho u_i u_j + p\delta_{ij} - \mu\frac{\partial u_j}{\partial x_i} + \mu\frac{2}{3}\delta_{ij}\frac{\partial u_{k\neq j}}{\partial x_{k\neq j}}\right) \rightarrow \text{Dirichlet when } i \neq j,$$
$$-\frac{\partial}{\partial x_j}\left(\rho u_i u_j + p\delta_{ij} - \mu\frac{\partial u_j}{\partial x_i} + \mu\frac{2}{3}\delta_{ij}\frac{\partial u_{k\neq j}}{\partial x_{k\neq j}}\right) \rightarrow \text{Neumann when } i = j, \text{ set } \rho u_i u_j + \mu\frac{2}{3}\delta_{ij}\frac{\partial u_{k\neq j}}{\partial x_{k\neq j}} = 0,$$
$$-\frac{\partial}{\partial x_j}\left[u_j(\rho E + p) - \mu u_i\frac{\partial u_j}{\partial x_i} + \mu u_i\frac{2}{3}\delta_{ij}\frac{\partial u_{k\neq j}}{\partial x_{k\neq j}}\right] \rightarrow \text{Dirichlet}, \; \frac{\partial}{\partial x_j}(-\rho u_j Y) \rightarrow \text{Dirichlet}$$

and the pure diffusion term numerical BCs are

$$\frac{\partial^2 u_i}{\partial x_j^2} \rightarrow \text{Neumann when } i \neq j, \text{ Dirichlet when } i = j,$$
$$\frac{\partial^2 Y}{\partial x_i^2} \rightarrow \text{Neumann},$$
$$\frac{\partial^2 T}{\partial x_i^2} \rightarrow \text{Neumann}$$

This gives us the correct way to apply BC to the compact finite differences. The Neumann condition is enforced directly through the matrix, and reflective ghost points are used to enforce the zero derivative at the boundary node ($f_{-1} = f_1$, etc.). The first-derivative matrix is

$$A_{1,Neumann} = \begin{bmatrix} 1 & 0 & 0 & 0 & \dots & 0 & 0 \\ \alpha & 1 & \alpha & 0 & \dots & 0 & 0 \\ 0 & \alpha & 1 & \alpha & \dots & 0 & 0 \\ \vdots & \vdots & \ddots & \ddots & \ddots & \vdots & \vdots \\ 0 & 0 & \dots & \alpha & 1 & \alpha & 0 \\ 0 & 0 & \dots & 0 & \alpha & 1 & \alpha \\ 0 & 0 & \dots & 0 & 0 & 0 & 1 \end{bmatrix}, \quad b_{1,Neumann} = \begin{bmatrix} 0 \\ \frac{a}{2h}(f_3 - f_1) + \frac{b}{4h}(f_4 - f_2) \\ \frac{a}{2h}(f_4 - f_2) + \frac{b}{4h}(f_5 - f_1) \\ \vdots \\ \frac{a}{2h}(f_{N-1} - f_{N-3}) + \frac{b}{4h}(f_N - f_{N-4}) \\ \frac{a}{2h}(f_N - f_{N-2}) + \frac{b}{4h}(f_{N-1} - f_{N-3}) \\ 0 \end{bmatrix}$$

Only a fourth-order stencil is used because that is the most accurate first derivative one-sided stencil provided by Lele [8]. The coefficients are $\alpha = 1/4, a = 2(\alpha + 2)/3, b = (4\alpha - 1)/3$. The second-derivative matrix requires a one-sided stencil,

$$A_{2,Neumann} = \begin{bmatrix} 1 & \alpha_s & 0 & 0 & \dots & 0 & 0 \\ \alpha & 1 & \alpha & 0 & \dots & 0 & 0 \\ 0 & \alpha & 1 & \alpha & \dots & 0 & 0 \\ \vdots & \vdots & \ddots & \ddots & \ddots & \vdots & \vdots \\ 0 & 0 & \dots & \alpha & 1 & \alpha & 0 \\ 0 & 0 & \dots & 0 & \alpha & 1 & \alpha \\ 0 & 0 & \dots & 0 & 0 & \alpha_s & 1 \end{bmatrix}$$

$$b_{2,Neumann} = \begin{bmatrix} \frac{1}{h^2}\left(a_s f_1 + b_s f_2 + c_s f_3 + d_s f_4 + e_s f_5\right) \\ \frac{a}{h^2}(f_3 - f_2 + f_1) + \frac{b}{4h^2}(f_4 - f_2 + f_2) + \frac{c}{9h^2}(f_5 - f_2 + f_3) \\ \frac{a}{h^2}(f_4 - f_3 + f_2) + \frac{b}{4h^2}(f_5 - f_3 + f_1) + \frac{c}{9h^2}(f_6 - f_3 + f_2) \\ \frac{a}{h^2}(f_5 - f_4 + f_3) + \frac{b}{4h^2}(f_6 - f_4 + f_2) + \frac{c}{9h^2}(f_7 - f_4 + f_1) \\ \vdots \\ \frac{a}{h^2}(f_{N-2} - f_{N-3} + f_{N-4}) + \frac{b}{4h^2}(f_{N-1} - f_{N-3} + f_{N-5}) + \frac{c}{9h^2}(f_N - f_{N-3} + f_{N-6}) \\ \frac{a}{h^2}(f_{N-1} - f_{N-2} + f_{N-3}) + \frac{b}{4h^2}(f_N - f_{N-2} + f_{N-4}) + \frac{c}{9h^2}(f_{N-1} - f_{N-2} + f_{N-5}) \\ \frac{a}{h^2}(f_N - f_{N-1} + f_{N-2}) + \frac{b}{4h^2}(f_{N-1} - f_{N-1} + f_{N-3}) + \frac{c}{9h^2}(f_{N-2} - f_{N-1} + f_{N-4}) \\ -\frac{1}{h^2}\left(a_s f_N + b_s f_{N-1} + c_s f_{N-2} + d_s f_{N-3} + e_s f_{N-4}\right) \end{bmatrix}$$

The coefficients for fourth-order central second derivative are $\alpha = 1/10, a = 12/11, b = 3/11, c = 0$ and for fourth-order one-sided second derivative are $\alpha_s = 1/10, a_s = 7, b_s = -104/5, c = 114/5, d = -56/5, e = 0$. For Dirichlet conditions, since the value at the node are enforced to be zero, we can apply odd reflection to obtain the ghost states ($f_{-1} = -f_1$). Since the derivative at the boundary is unknown, we must use a one-sided stencil for Dirichlet BC. The Matrix-vector system for the first derivative will look like

$$A_{1,Dirichlet} = \begin{bmatrix} 1 & \alpha_s & 0 & 0 & \dots & 0 & 0 \\ \alpha & 1 & \alpha & 0 & \dots & 0 & 0 \\ 0 & \alpha & 1 & \alpha & \dots & 0 & 0 \\ \vdots & \vdots & \ddots & \ddots & \ddots & \vdots & \vdots \\ 0 & 0 & \dots & \alpha & 1 & \alpha & 0 \\ 0 & 0 & \dots & 0 & \alpha & 1 & \alpha \\ 0 & 0 & \dots & 0 & 0 & \alpha_s & 1 \end{bmatrix},$$

$$b_{1,Dirichlet} = \begin{bmatrix} \frac{1}{h}(a_s f_1 + b_s f_2 + c_s f_3 + d_s f_4 + e_s f_5) \\ \frac{a}{2h}(f_3 - f_1) + \frac{b}{4h}(f_4 + f_2) \\ \frac{a}{2h}(f_4 - f_2) + \frac{b}{4h}(f_5 - f_1) \\ \vdots \\ \frac{a}{2h}(f_{N-1} - f_{N-3}) + \frac{b}{4h}(f_N - f_{N-3}) \\ \frac{a}{2h}(f_N - f_{N-2}) + \frac{b}{4h}(-f_{N-1} - f_{N-2}) \\ -\frac{1}{h}(a_s f_N + b_s f_{N-1} + c_s f_{N-2} + d_s f_{N-3} + e_s f_{N-4}) \end{bmatrix}$$

The one-sided first derivative coefficients for fourth-order accuracy are $\alpha_s = 3, a_s = -17/6, b_s = 3/2, c_s = 3/2, d_s = -1/6, e_s = 0$. Second-derivative matrix also requires a one-sided stencil, with the same matrix form (but different coefficient values) as the second derivative with Neumann

$$b_{2,Dirichlet} = \begin{bmatrix} \frac{1}{h^2}\left(a_s f_1 + b_s f_2 + c_s f_3 + d_s f_4 + e_s f_5\right) \\ \frac{a}{h^2}(f_3 - f_2 + f_1) + \frac{b}{4h^2}(f_4 - f_2 - f_2) + \frac{c}{9h^2}(f_5 - f_2 - f_3) \\ \frac{a}{h^2}(f_4 - f_3 + f_2) + \frac{b}{4h^2}(f_5 - f_3 + f_1) + \frac{c}{9h^2}(f_6 - f_3 - f_2) \\ \frac{a}{h^2}(f_5 - f_4 + f_3) + \frac{b}{4h^2}(f_6 - f_4 + f_2) + \frac{c}{9h^2}(f_7 - f_4 + f_1) \\ \vdots \\ \frac{a}{h^2}(f_{N-2} - f_{N-3} + f_{N-4}) + \frac{b}{4h^2}(f_{N-1} - f_{N-3} + f_{N-5}) + \frac{c}{9h^2}(f_N - f_{N-3} + f_{N-6}) \\ \frac{a}{h^2}(f_{N-1} - f_{N-2} + f_{N-3}) + \frac{b}{4h^2}(f_N - f_{N-2} + f_{N-4}) + \frac{c}{9h^2}(-f_{N-1} - f_{N-2} + f_{N-5}) \\ \frac{a}{h^2}(f_N - f_{N-1} + f_{N-2}) + \frac{b}{4h^2}(-f_{N-1} - f_{N-1} + f_{N-3}) + \frac{c}{9h^2}(-f_{N-2} - f_{N-1} + f_{N-4}) \\ -\frac{1}{h^2}\left(a_s f_N + b_s f_{N-1} + c_s f_{N-2} + d_s f_{N-3} + e_s f_{N-4}\right) \end{bmatrix}$$

Again, the central and one-sided second derivative uses the same coefficients as before.

References

[1] C.S. Bender et al. *Characterization of Rayleigh-Taylor Instabilities Induced by Volumetric Energy Deposition.* International Modal Analysis Conference (IMAC). LA-UR-25-21059. Orlando, Florida, United States, Feb. 2025.

[2] S. Diot and M.M. François. "An interface reconstruction method based on an analytical formula for 3D arbitrary convex cells". In: *Journal of Computational Physics* 305 (2016), pp. 63–74.

[3] M.B. Giles. "Stability analysis of numerical interface conditions in fluid–structure thermal analysis". In: *International journal for numerical methods in fluids* 25.4 (1997), pp. 421–436.

[4] M. Gittings et al. "The RAGE radiation-hydrodynamic code". In: *Computational Science & Discovery* 1.1 (2008), p. 015005.

[5] Y. Guo and Y. Han. "Critical rayleigh number in rayleigh-bénard convection". In: *Quarterly of Applied Mathematics* 68.1 (2010), pp. 149–160.

[6] D.W Hahn and M.N Özisik. *Heat conduction.* John Wiley & Sons, 2012.

[7] Z. Jibben et al. "Modeling surface tension in compressible flow on an adaptively refined mesh". In: *Computers & Mathematics with Applications* 78.2 (2019), pp. 504–516.

[8] S.K. Lele. "Compact finite difference schemes with spectral-like resolution". In: *Journal of computational physics* 103.1 (1992), pp. 16–42.

[9] D. Livescu, T. Wei, and M.R. Petersen. "Direct numerical simulations of Rayleigh-Taylor instability". In: *Journal of Physics: Conference Series.* Vol. 318. 8. IOP Publishing. 2011, p. 082007.

[10] W.J. Rider and D.B. Kothe. "Reconstructing volume tracking". In: *Journal of computational physics* 141.2 (1998), pp. 112–152.

[11] P.T. Root et al. "Design of Rayleigh-Taylor instability experiments driven by volumetric energy deposition". In: *ASTFE Digital Library.* Begel House Inc. 2025.

[12] D.E. Ruiz. "Degradation of performance in ICF implosions due to Rayleigh–Taylor instabilities: A Hamiltonian perspective". In: *Physics of Plasmas* 31.12 (2024).

[13] A.J. Wachtor et al. "On buoyancy driven mixing by volumetric microwave energy deposition". In: *International journal of heat and mass transfer* 86 (2015), pp. 443–454.

[14] J.T. Waddell, C.E. Niederhaus, and J.W. Jacobs. "Experimental study of Rayleigh-Taylor instability: low Atwood number liquid systems with single-mode initial perturbations". In: *Physics of Fluids* 13.5 (2001), pp. 1263–1273.